*Final Draft*
**of the original manuscript:**

Bystrzanowski, S.; Bartels, A.; Stark, A.; Gerling, R.; Schimansky, F.-P.; Clemens, H.:

**Evolution of microstructure and texture in Ti–46Al–9Nb sheet material during tensile flow at elevated temperatures**

In: Intermetallics ( 2010) Elsevier

DOI: 10.1016/j.intermet.2010.01.036

# Evolution of microstructure and texture in Ti-46Al-9Nb sheet material during tensile flow at elevated temperatures

**S. Bystrzanowski[a], A. Bartels[a], A. Stark[b*], R. Gerling[b], F.-P. Schimansky[b], H. Clemens[c]**

[a]Institute of Materials Science and Technology, Hamburg University of Technology, D-21073 Hamburg, Germany

[b]Institue of Materials Research, GKSS Research Centre, Max-Planck-Str. 1, D-21502 Geesthacht, Germany

[c]Department of Physical Metallurgy and Materials Testing, Montanuniversität Leoben, A-8700 Leoben, Austria

[*]*Corresponding author. Tel.: +49 4152 87-2663; fax: +49 4152 87-2534*

*E-mail address: andreas.stark@gkss.de*

**Abstract:**

Microstructure and texture evolution as well as phase transformations in Ti-46Al-9Nb sheet material tensile tested between 700 and 1000°C have been analyzed. Up to ~850°C the microstructure shows characteristic deformation features such as mechanical twins and deformation bands. The texture, presented as inverse pole figures, contains pure deformation components, i.e. <001>, <111> and ~<301>. Above 900°C dynamic recrystallization becomes the dominant process. Bulged grain boundaries can clearly be distinguished in the microstructure of the tensile specimens, and the pure deformation orientation maxima <001> and <301> disappear from the texture map in favor of a new recrystallization component around <100>. Under constant temperature conditions the size of dynamically recrystallized grains is influenced by the applied strain rate. Under certain test conditions a $\alpha_2 \rightarrow \omega/B8_2$

phase transformation can be observed. This process is enhanced by stress and depends strongly on temperature and time or strain rate.

**Keywords:**

A. Titanium aluminides, based on TiAl; B. Phase transformation; B. Texture; D. Deformation induced microstructure; F. Texture

## 1. Introduction:

High Nb containing γ-TiAl based alloys, called TNB-alloys throughout this paper, belong to the most promising light-weight structural materials for use in aerospace and automotive applications at temperatures in the range of ~650 to 800°C. As a consequence of high Nb concentrations their tensile- and creep-strength as well as their oxidation resistance are significantly improved with respect to TiAl alloys possessing low Nb contents. Therefore, several investigations were conducted in order to examine the influence of large Nb additions on strengthening, phase transformations and microstructure in TNB-alloys [1-5]. Hitherto, however, plastic deformation of such alloys and related effects as strain hardening, dynamic recrystallization or texture development have not been in the center of interest, although knowledge of such processes is important for applications [6]. In a recent paper we have reported about such properties in Ti-46Al-9Nb (all compositions in atomic percent) sheet material [7]. The sheet material has been powder metallurgically processed and tensile tested in the temperature range of 700 to 1000°C using three different strain rates at each selected temperature. In addition, strain rate jump tests were performed. From the resulting stress/strain curves parameters as yield stress, fracture strain, activation volumes, and strain hardening curves were derived. The most important results from that investigation can be summarized as follows:

- With respect to the stress/strain characteristics as strain hardening and stress exponents, this ordered intermetallic alloy behaves at elevated temperatures to some extend like conventional bcc or fcc metals. The flow behaviour and ductility shows a strong dependence on temperature and strain rate and above 800°C a drastic increase in plasticity was observed.
- The variation of the activation volume with temperature indicated the growing role of thermally activated climb processes between 750 and 825°C and the onset of dynamic recrystallization around 900°C. Additionally, the obtained activation enthalpy indicated phase transformations and a related development of the $\omega/B8_2$-phase at intermediate stresses and temperatures.

The basis for the present paper is the same material as used in ref. [7], which was tensile tested until failure at temperatures from 700 to 1000°C using different strain rates. The main subject for the investigations was the change of the microstructure and texture during tensile testing. Since a new phase, the $\omega/B8_2$-phase, which has not been present in the initial sheet material, developed under certain test conditions, results concerning formation kinetics are also included in this paper.

## 2. Experimental

The sheet material used for these investigations was hot rolled from powder compacts [8]. Ti-46Al-9Nb alloy powder was produced by means of plasma melting induction guiding gas atomization [9]. The powder with a size fraction in the range of 0 to 180 micrometer was hot isostatically pressed for 2h at 1270°C and 200MPa and the resulting dense powder compacts were hot rolled to sheets at Plansee SE, Austria. The dimensions of the sheets ranged around $600x300x1.2mm^3$. In order to flatten the sheets, to reduce internal stresses and to stabilize the microstructure, the sheets were primary annealed for 3h at 1000°C.

Tensile test specimens, with gauge lengths and widths of 45 and 5mm, respectively, were prepared in rolling direction of the sheets. Tensile tests were carried out until failure in the range of 700 to 1000°C using 50°C increments. For each temperature three different strain rates between $1x10^{-6}$ and $1x10^{-3}$ $s^{-1}$ were applied. The exact test conditions as temperature and strain rate along with the fracture elongation are listed in Table 1 and are related to the inverse pole figures discussed later on in Fig. 6. A Zwick 1474 tensile test machine was used for these experiments. For an exact control of the temperature a three zone pipe furnace has been used. The sample temperature was measured by two thermocouples positioned at both ends of the specimens. All tests were conducted in air. In order to achieve a constant strain rate, the cross head speed was computer-controlled. Immediately after failure of the sample, the furnace was opened and the specimen was rapidly cooled to RT by pressurized air. By doing so, both the deformation microstructure and texture were preserved.

The microstructural characterization was performed by polarized light microscopy (LM) using a Leica ARISTOMET equipped with a high sensitive Hamamatsu CCD-camera. In addition scanning electron microscopy (SEM) techniques with a LEO 1530 Gemini (FEGSEM) were used. The specimens were prepared by mechanical grinding and polishing using a RotoPol 31 grinding-polishing machine. In order to improve the contrast for the SEM analysis conducted in back-scatter electron mode (BSE) the specimens were electrolytically polished. Microstructural examinations were conducted in the direction normal to the surface of the sheets. Different parts of the tested specimens, i.e. non-deformed head sections and regions of uniform deformation as well as necking-zones, were thoroughly analyzed.

Phase analyses was conduced by means of a X-ray Diffractometer - D8 Advance, Bruker Analytical X-ray Systems (AXS), using a Bragg-Brentano technique. Additionally, the device was modified with a Bragg-Brentano mirror, which cuts off the Cu-$K_\beta$-radiation and provides a monochromatic Cu-$K_\alpha$-radiation. The measurements were performed between $2\Theta = 20° - 85°$. For the analysis of the results and identification of phases, Diffrac Plus, EVA evaluation

software as provided by Bruker AXS was used. For additional phase identification electron back-scattered diffraction (EBSD) was applied. For these measurements a Zeiss EV050 SEM equipped with an Oxford Instruments Inca Crystal 300 System was employed.

For the measurement of the textures different sample geometries were used. For the texture analysis of the initial sheet material, a sample with dimensions of 21× 20 $mm^2$ was prepared, whereas for textures measurements of the differently stressed and strained specimens, the gauge regions were cut in three sections, each about 13 mm in length. Then the three sections were arranged parallel to each other forming a sample of approx. 15×13 $mm^2$ in size. Before measuring the surfaces of all specimens were prepared by mechanical grinding and polishing. The texture measurements were performed by X-ray diffraction (XRD) in reflection geometry with filtered Cu-$K_\alpha$-radiation using a texture goniometer with Eulerian cradle and parallel beam optic - D8 Discover from Bruker AXS. Due to the parallel beam technique a very low background level and a high peak resolution even at polar angles up to 85° is achieved and allows the seperate measuring of pole figures [10]. Among with the strong {111} reflection, also the relatively weak superlattice reflections (001), {110} and {201} of the tetragonal $L1_0$-ordered γ-TiAl phase (space group: P4/mmm) were used in this study. The measured incomplete pole figure were subsequently corrected for background and intensity loss. Correction factors for intensity loss were obtained from measurements of HIPed powder specimens with a random orientation. The orientation distribution function (ODF) of the γ-phase was calculated by employing the harmonic series expansion method [11, 12] up to an order of 22. The inverse pole figures discussed in section 3.3 were recalculated from the ODF

## 3. Results and discussion

### *3.1 Evolution of microstructure*

The microstructure of the initial material is shown as LM and SEM-BSE images in Figs. 1a and b. The near gamma microstructure consists of areas of globular γ-TiAl grains with a grain size in the range of 10 to 15μm. The globular γ-grains are surrounded by areas of the Chinese script type consisting of small (~1 - 3μm) γ-TiAl grains and plate-like $\alpha_2$-$Ti_3Al$ particles. These areas are formed during the primary annealing of the sheets (3 hours at 1000°C) by a transformation of surplus $\alpha/\alpha_2$-grains which are present after rolling at higher temperatures and subsequent fast cooling to room temperature.

In the first experimental series specimens were deformed at a constant strain rate of $1x10^{-4}$ $s^{-1}$, but at different temperatures. Subsequent to the tensile tests the specimens were investigated by means of LM and SEM in BSE mode. Examples for the resulting microstructures of the uniformly deformed regions are presented in Figs. 1c - 1h.

During tensile testing at 750°C the material shows a low ductility with a plastic elongation to fracture of about 0.05 (for plastic elongations see also Tab. 1). After such a small strain to fracture the microstructure remains nearly unchanged, however, some grains exhibit significant amounts of deformation twins (Figs. 1c,d; in Fig. 1c deformation twins are marked by arrows ) when compared to the initial material (Fig. 1a,b). This indicates that mechanical twining is a very active deformation mode under these test conditions. An increase in temperature up to 850°C leads to an increased tensile ductility. In this case the specimen experienced a true elongation of 0.46. Consequently, drastic changes in the microstructure are observed (Figs. 1e and f). Most grain boundaries show a curvature (bulging) and small new grains occur at the grain boundaries (necklacing). This is commonly observed in the early stages of dynamic recrystallization (DRX) [13, 14]. A close inspection of the BSE-image (Fig.1f) indicates that apart from the γ-TiAl phase (darkest contrast) and the $\alpha_2$-$Ti_3Al$ phase (grey-like contrast) a further small amount of fine particles has been formed. The precipitates are about 0.5 – 1μm in size and show the brightest (white) BSE contrast, pointing at a different chemical composition when compared to the well known phases γ-TiAl and $\alpha_2$-

$Ti_3Al$. As will be shown in the next section these precipitates can be identified by means of X-ray diffraction and EBSD as $\omega/B8_2$-phase. It is worth noting that these precipitates are not visible in the SEM images taken from specimens tensile tested with a strain rate of $1\times10^{-4}$ $s^{-1}$ at 750°C and 1000°C (Figs. 1d and h). Both LM and BSE images (Figs. 1g and h) of the microstructure, which developed during tensile deformation at 1000°C up to $\varepsilon = 0.65$, suggest that dynamic recrystallization is highly advanced, but not finished in the sense of reaching a steady state condition. In both LM and BSE figures newly recrystallized $\gamma$-grains, ~ 4 – 7µm in size, can clearly be distinguished. Some of the grains exhibit regular, almost planar, grain boundaries indicating that the grains have achieved their "equilibrium" shape with reduced grain boundary energy by minimizing the grain boundary area. Other grains still show a bulged morphology indicating a proceeding process of grain boundary migration. The high density of mechanical twinning, the appearance of deformation/shear bands as well as the tendency to dynamic recrystallization, as observed in this study, are characteristic for "fcc" metals with low stacking fault energy [15, 16]. Since Nb is known to reduce the stacking fault energy of TiAl alloys significantly [17-19], it is primarily the Nb concentration which is seen to be responsible for the above mentioned phenomena.

In the second experimental series, tensile tests were conducted at each temperature using two further strain rates (see Tab. 1). Figs. 2a to d show an example for the variation of the microstructure with strain rate. Both samples were tested at 950°C and experienced an almost identical amount of deformation ($\varepsilon \sim 0.47$). The time, however, in which this degree of deformation was achieved, differs by a factor of 10. The sample tested with the higher strain rate, i.e. $1\times10^{-3}$ $s^{-1}$, shows many strongly deformed grains (Fig. 2a). In contrast, the microstructure of the specimen tested at $1\times10^{-4}$ $s^{-1}$ contains a large amount of dynamically recrystallized grains with bulged grain boundaries (Fig. 2b). This indicates a strong dependence of DRX on strain rate. Figs. 2c and d show the microstructure in the necking

regions of these samples. For both strain rates the microstructure is much finer and exhibits a larger volume fraction of small recrystallized grains when compared to the uniformly deformed specimens. The reason for this are different deformation conditions: Near the neck the material is deformed at a much higher local strain rate and, therefore, experiences a significantly larger degree of deformation if compared to the uniformly deformed part of the gauge. Thus, in the neck more energy is stored, promoting recrystallization processes.
The process of dynamic recrystallization can clearly be seen in microstructural images, e.g. Figs. 1 and 2. In recent investigations using the same samples [7] the conditions for dynamic recrystallization were deduced from variations in the activation volume and the activation enthalpy as well as from characteristics of the stress/strain curves. In these investigations the range of temperature and strain rate conditions where the DRX process becomes the dominant one are determined independently. However, the obtained results are in good agreement. Further aspects concerning the DRX process will be discussed in the section "texture development".

*3.2 Formation of the ω/B8$_2$-phase*

As shown in the previous section BSE examinations indicated the formation of fine-grained precipitates under distinct tensile test conditions. EBSD measurements indicated these precipitates to consist of the ω/B8$_2$ or B2-phase. Obviously, the B2 or B8$_2$ structures are too similar in the EBSD pattern, thus an exact discrimination between these two phases is not possible. The same problem is known from the tetragonal γ-TiAl structure, which can be analyzed by EBSD only as fcc-structure since the tetragonality is very small. The recorded XRD spectra, however, gave no indication for the presence of the B2-phase. In conclusion, the EBSD experiments gave evidence that the bright appearing precipitates are definitely no α$_2$-phase, but either ω/B8$_2$ or B2. The XRD spectra clearly show ω-related diffraction peaks

and no evidence of B2-related peaks. The presence of the ω/$B8_2$-phase was proven in a temperature range from 700 to 850°C. As example, Fig. 3 shows three different X-ray spectra: (a) taken from the initial sheet material, (b) the gauge region of a sample tensile strained at 750°C to ε = 0.46 using a strain rate of $1\times10^{-5}$ $s^{-1}$, and (c) the corresponding head of the tested sample which experienced no mechanical stress at 750°C. The reflections originating from the ω/$B8_2$-phase are clearly visible in the gauge area of the sample. In the non-stressed head of the tensile specimen the ω-related reflections are very small and the ω-phase is seen to be not existent in the initial sheet material.

In order to discuss the formation conditions of the ω-phase the results of the X-ray diffraction measurements conducted on the gauge area of all samples are compiled in Fig. 4. For each temperature three tensile tests were conducted at three different strain rates until failure. In Fig. 4 the duration of the respective tensile test is plotted over the temperature and the presence or absence of the ω/$B8_2$-phase after the experiment is indicated. Fig. 4 shows the range of time and temperature where the ω-phase could be identified. For example, at temperatures above 850°C the ω-phase does not appear, irrespective of the duration of the experiment.

The diffraction spectra (b) and (c) in Fig. 3 show that the ω/$B8_2$-phase was mainly found in the stressed gauge area and only after a long time of deformation it appears also in the unstressed head of the sample. For example, at 750°C the ω-related reflections are well developed in the stressed parts of two samples with the longer time of deformation (> 1h, Fig. 4), while in the corresponding stress-free head sections the ω related diffraction peaks are still very small even after 11.7h exposure to 750°C (Fig. 3c). EBSD analyses of the gauge and head-sections of the sample tested at 750°C at a strain rate of $1\times10^{-5}$ $s^{-1}$ indicated ω-phase fractions of around 10 vol% and < 1 vol%, respectively. Qualitatively, this is in good agreement with the intensity of the diffraction peaks (Fig. 3, compare b to c). Fig 5 shows the

microstructure in the head and gauge area of that sample. In the microstructure of the gauge area, Fig. 5 bottom, the ω-phase, characterized by the brightest white contrast, is indicated by an arrow. Again the ω-phase fraction seems to be much higher in the stressed part of the sample if compared to the stress-free head. Thus, the formation of the ω-phase is strongly favored by the presence of stress and/or the induced strain. This is supported by comparing the results of this study with those derived from creep experiments [20]: After a 50h tensile test at 700°C the ω-phase could be identified, while after a 100h creep test at the same temperature the ω-phase was missing. The reason is seen in the different stresses which were applied and/or the different achieved strains. They ranged around 500MPa and $\varepsilon = 0.18$ during the tensile test, in contrast to 225MPa and $\varepsilon = 0.006$ during the creep experiment.
As can be seen in Fig. 3 for the sample tested at 750°C, the raise of ω-peaks is accompanied by a decrease of the $\alpha_2$ related peaks (e.g., see $\alpha_2$-(201) at 40.8°). This correlation is found in all cases where the ω-phase occurred and indicates that the ω-phase grew in expense of the $\alpha_2$-phase. The driving force for the decrease of the $\alpha_2$ volume fraction probably lies in the accelerated cooling after the final sheet rolling step. Therefore, despite the primary annealing for 3 hours at 1000°C, the near gamma sheet material contains an $\alpha_2$-volume fraction which is still in excess of that expected for thermodynamic equilibrium at the test conditions used in this study. An $\alpha_2$-volume fraction in excess of thermodynamic equilibrium was also noticed in a recent "in situ" high-energy X-ray diffraction study. Ti-45Al-7.5Nb alloy powder was hot isostatically pressed and furnace cooled at the end of the compaction process. During subsequent annealing, the $\alpha_2$-volume fraction started to decrease at about 750°C, while the γ-phase fraction slightly increased [21]. The occurrence of the ω/$B8_2$-phase in γ-TiAl based alloys has already been confirmed by several authors who investigated alloys with relatively low Al concentrations and usually high Nb additions: e.g. Ti-37.5Al-12.5Nb [22], Ti-40Al-10Nb [23] and Ti-45Al-10Nb [19, 24]. In those alloys a certain amount of a β/B2-phase has

always been retained in the metastable state as a result of high cooling rates during the fabrication process, leading to non-equilibrium phase conditions. Subsequently, a long-term annealing or an intermediate-temperature deformation leads to the formation of the $\omega/B8_2$-phase. Bendersky et al. [22] have proposed a transformation path for the formation of the ω-phase in Ti-37.5Al-12.5Nb according to: $\beta/B2 \rightarrow \omega'' \rightarrow \omega/B8_2$, where ω" is an intermediate trigonal phase. According to Sikka et al. [25] the transformation of the $\alpha/\alpha_2$-phase into the ω-phase can also proceed via an intermediate $\beta/B_2$-phase, i.e. $\alpha/\alpha_2 \rightarrow \beta/B2 \rightarrow \omega/B8_2$. In our case, no evidence for the presence of the β/B2-phase in the initial material can be given, however, the ω-phase is formed as well. Recent Calphad calculations of the free energy curves for individual phases have shown that from the thermodynamic point of view the phase transformation reaction such as $\alpha/\alpha_2 \rightarrow \beta/B2 \rightarrow \omega/B8_2$ is unlikely, since the free energy curve for the $\alpha_2$-phase lies below that of the β/B2-phase. Thus, the transformation $\alpha/\alpha_2 \rightarrow \beta/B2$ would lead to an increase in free energy of the system. In the light of these results, the direct $\alpha/\alpha_2 \rightarrow \omega$ transformation is favored for the interpretation of the obtained experimental observations. The observed influence of applied stress on the formation of $\omega/B8_2$-phase is in agreement with another observation of Sikka et al. [25]. They have calculated and analyzed free energy curves for α-, β- and ω-phases for the group IV of transition metal elements and shown that at constant temperature the free energy curve for the ω-phase is considerably shifted to lower free energies when the pressure is increased, i.e. the free energy falls below those of the other phases and thus the ω-phase becomes the most stable one.

*3.3 Texture development and texture simulation of γ-TiAl*

The development of texture during the various tensile test experiments is summarized in Fig.6, where the re-calculated inverse pole figures in tensile direction are plotted. Inverse pole

figures provide information about the volume fraction of crystals with a given crystal direction parallel aligned to a specific test direction of the sample. Normally, during uniaxial deformation axially symmetric textures (i.e. fiber textures) are formed which are characterized by crystal directions <uvw> parallel to the deformation direction. In this case, the inverse pole figures in tensile direction [Fig 6] provide the complete texture information. The tensile direction in our experiments is always equivalent to the previous rolling direction (RD) of the starting sheet material. Quantitatively, the texture can be characterized by their maximum intensity level number (plotted in the left-upper corner of every individual inverse pole figure in Fig. 6), which describes how many times a given texture is stronger than a perfect random texture, characterized by a value of 1.

In our experiments the starting texture (Fig. 6a and Fig. 7a) is not completely random, but represents a weak recrystallization texture, which has been developed during hot-rolling and subsequent primary annealing (described in detail in [7]). The texture is distinguished by a weak modified cube component {100}<010>, which is one of three possible tetragonal variants of the cube component known from cubic materials [26]. In Fig. 6a this component can be recognized by the slight accumulation of orientations around the <100> direction showing a maximum intensity level of ~1.5 times random. The modified cube component does not withstand uniaxial deformation as can be deduced from the following inverse pole figures in Fig. 6. In addition, this is ilustrated in Fig. 7. Already after a true strain of 0.15 the development of a typical axially symmetric texture can be observed and the weak starting texture disappeared (Fig. 7b), and after higher strains (Fig. 7c) a distinct fiber texture is formed. The inverse pole figures in Fig. 6 demonstrate that the crystallites change their initial orientation during tensile straining and rotate into new positions depending on temperature and strain rate. As a result, at first a broad orientation maximum is developed between <100> and <301> at small deformation degrees.(Figs. 6b to 6e) and, eventually, a more distinct/sharp orientation maximum is created around <301> at large deformations (Figs. 6f to 6j). Apart

from that, two other orientation maxima can be recognized and characterized as deformation components. The first distinct maximum occurs around <111>, which points to an alignment of the {111} planes perpendicular to the tensile direction. The second deformation maximum is clearly recognized around <001> and can be attributed to mechanical twinnng as discussed and numerically simulated below. Both, <111> and <001> orientation maxima appear also as the typical ones in textures of "fcc" materials, which are closely related to the $L1_0$ ordered γ-TiAl, after uniaxial elongation, such as wire drawing, extrusion, tension, and forging [27]. Moreover, it is known that the relative "amount" of <111> and <001> components, produced by uniaxial deformation, depend on deformation temperature and, also, on the stacking fault energy of the material [27]. For example, the strength of the <001> component increases with decreasing stacking fault energy or decreasing deformation temperature. Such a behavior has been attributed to the growing role of mechanical twinning [27]. Though the tetragonal TiAl structure has only one <001> main axis compared to three symmetrically equivalent main axis of cubic structures, a similar behavior can be observed.

With a successive increase of the test temperature the texture undergoes significant changes as reflected in Figs. 6j to 6r. The <001> component vanishes systematically when the temperature is increased or, alternatively, when the strain rate is decreased. A possible reason for this behavior can be the fact that at higher temperatures and lower strain rates activation of mechanical twinning becomes difficult, since the flow stress of the material is considerably reduced [7]. Therefore, the <001> component, which occurs mainly due to the twinning, is weaker under these conditions. This behavior is especially well seen at 900°C (Figs. 6j to 6l) and 950°C (Figs. 6m to 6o). The total elongation for the three strain rates and the two temperatures is comparable, whereas the strength of the <001> component changes noticeably. For example, at 950°C and after tension with the strain rate of $1\times10^{-3}$ $s^{-1}$ a most pronounced maximum is observed (Fig. 6m). After testing with $3\times10^{-4}$ $s^{-1}$ the maximum is significantly weaker (Fig. 6n). Eventually, it vanishes completely after tension with the rate of

$1\times10^{-4}$ $s^{-1}$ (Fig. 6o). Here, the decreasing strain rate corresponds directly to a lower level of the flow stress (for details see Table 1 in [7]).

It should also be noted that with an increase of temperature and a decrease of strain rate (or in other words with an increase of deformation time), dynamic recrystallization proceeds and plays a more dominant role. Such behavior is expected since DRX starts at a certain temperature and needs, apart from sufficient amount of stored deformation energy, sufficient time for nucleation and subsequent nucleus growth. Consequently, DRX influences the deformation texture and also contributes to the degradation of the <001> component. Moreover, the proceeding DRX is reflected in the disappearance of the orientation maximum around <301> and the re-creation of the orientation maximum around <100>, which is also observed in the initial recrystallization texture.

The tendency to re-build the <100> component increases with an increase of temperature and time of deformation, which correlates undoubtedly to the higher volume fraction of recrystallized material. The effect of strain rate (corresponds to deformation time) on the occurrence of DRX, which has been evidenced by means of texture measurements were also confirmed by the microstructural observations ( see Section 3.1). Another feature which is recognized in the texture developed at higher temperatures (generally above 900°C) is the fact that the broad orientation maximum around <111> still exists. This suggests that the <111> deformation component is stable against recrystallization and/or is also formed during DRX.

The texture development during uniaxial deformation was simulated numerically in a Taylor-type simulation using the Los Alamos poly plasticity (LApp) code [28]. The simulation is based on the model of the single crystal yield surface of $L1_0$ ordered γ-TiAl according to Mecking et al. [29]. The model utilizes a classical Bishop-Hill theory for plastic deformation, where the shear processes activated in a grain by external and internal stresses are defined by the shape of the yield surface [29, 30]. In general, the shear processes in TiAl can be realized by means of 4 ordinary dislocation slip systems, 8 superdislocation slip systems and 4 uni-

directional twinning systems, which create a yield surface body in the five-dimensional stress hyperspace (represented by two deviatoric and three shear stresses) [26]. The shape of the yield surface body is exclusively determined by the ratios of the critical resolved shear stresses (CRSS) for ordinary dislocation and superdislocation slip ($\tau_o/\tau_s$) and for twinning and superdislocation slip ($\tau_t/\tau_s$). Depending on these ratios, 13 different regimes can be defined in the deformation mode map of polycrystalline TiAl with a random texture [29] These regimes are distinguished by different contributions of ordinary and superdislocations as well as mechanical twinning to the total deformation process. The simulation of the texture development during tensile deformation calculated with CRSS ratios of $\tau_o/\tau_s = 0.9$ and $\tau_t/\tau_s = 0.4$ shows the best concordance with the experiments (Fig. 8). These ratios correspond to a regime in Mecking's deformation mode map, that shows a contribution to the total deformation of 39%, 33%, and 28% for ordinary dislocation, superdislocation, and twinning, respectively [29]. The simulation was done stepwise by small strain steps of $\varepsilon = 0.02$. Fig. 8a shows the orientation flow during tensile deformation, calculated for the step between 0 and 0.02. Already at the beginning of the deformation an oriented flow towards <111>, <001> and <301> is observed (arrowed maxima). In Fig. 8b, corresponding to the next deformation step (between 0.02 and 0.04), a significant twinning activity can additionally be recognized as thin arrowed lines directing towards <001>. In the course of deformation more and more orientations in the triangle <100>-<111>-<110> rotate towards <111> and are subsequently shifted towards <001> by twinning. This finding can explain the low orientation density in this triangle and confirms that the maximum at <001> occurs mainly due to mechanical twinning. A comparison of the theoretical predictions (Figs. 8a and b) with an experimental result (Fig. 8c) shows a very good qualitative agreement. Finally, it should be stated that a parameter combination of $\tau_o/\tau_s = 0.9$ and $\tau_t/\tau_s = 0.4$ is an optimal choice for modeling the orientation flow during tensile deformation of TiAl.

## 4. Conclusions

In this study the evolution of microstructure and texture in Ti-46Al-9Nb sheet material during tensile flow have been investigated in the temperature range of 700°C to 1000°C and the following conclusions can be drawn:

- At the lower range of the test temperature mechanical twins are already present in the microstructure after small degrees of deformation (e.g. $\varepsilon = 0.05$), which underline the significant role of this mechanism in tensile deformation of γ-TiAl based alloys.
- Through appropriate choice of deformation parameters, i.e. temperature and strain rate, it is possible to influence the kinetics of dynamic recrystallization and, thus, to control the grain size of the material.
- During deformation below 900°C a further solid-state phase transformation occurs. Here, an ω-related phase with $B8_2$-structure forms at the cost of dissolving $\alpha_2$-$Ti_3Al$ phase.
- The formation of the ω/$B8_2$-phase is enhanced by the presence of stress. Moreover, temperature and strain rate (in other words the time of the experiment) are also important factors for onset and amount of the ω/$B8_2$-phase.
- The proposed direct transformation path $\alpha_2 \rightarrow$ ω/$B8_2$ is in agreement with thermodynamic considerations.
- The formation of the tensile texture in tetragonal γ-TiAl can be described by similar mechanisms and texture components as they are typically known from uniaxial deformation processes of "fcc" metals.
- The texture components found experimentally can be simulated qualitatively using a Taylor type simulation, e.g. the LAPP code.

**References**

[1] Appel F, Wagner R. Mater Sci Eng 1998; R22: 187.

[2] Zhang WJ, Deevi SC, Chen GL. Intermetallics 2002; 10: 403.

[3] Zhang WJ, Appel F. Mater Sci Eng 2002; A329-331: 649.

[4] Zhang D, Dehm G, Clemens H. Z Metallkde 2000; 91: 950.

[5] Hu D. In: Lütjering G, Albrecht J, editors. Ti-2003 Science and Technology. vol. 4. Weinheim, Germany: Wiley-VCH; 2004. p. 2369.

[6] Paul JDH, Appel F. Metall Mater Trans A 2003; 34: 2103.

[7] Bystrzanowski S, Bartels A, Clemens H, Gerling R. Intermetallics 2008; 16: 717.

[8] Gerling R, Bartels A, Clemens H, Kestler H, Schimansky F-P. Intermetallics 2004; 12: 275.

[9] Gerling R, Clemens H, Schimansky F-P. Adv Eng Mater 2004; 6: 23.

[10] Schillinger W, Bartels A, Gerling R, Schimansky F-P, Clemens H. Intermetallics 2006; 14: 336.

[11] Bunge HJ. Texture analysis in materials science mathematical methods. London, Boston: Butterworths; 1982.

[12] Dahms M, Bunge HJ. Textures and Microstructures 1988; 10: 97.

[13] Mecking H, Gottstein G. In: Haessner F, editor. Recrystallization of Metallic Materials. Stuttgart, Germany: Riederer Verlag; 1978. p. 195.

[14] Cahn RW. In: Margolin H, editor. Recrystallization, Grain Growth and Textures. Metals Park, Ohio, USA: ASM; 1966. p. 109.

[15] Malin AS, Hatherly M. Metal Sci 1979; 13: 463.

[16] Morii K, Mecking H, Nakayama Y. Acta Metall 1985; 33: 379.

[17] Appel F, Oehring M, Wagner R. Intermetallics 2000; 8: 1283.

[18] Appel F. In: Schneibel JH, Hemker KJ, Noebe RD, Hanada S, Sauthoff G editors. High-

Temperature Ordered Intermetallic Alloys IX. Mater Res Soc Proc, vol. 646. Pittsburg, USA: MRS; 2001. p. N1.8.1.

[19] Chen GL, Zhang WJ, Liu ZC, Li SJ, Kim Y-W. In: Kim Y-W, Dimiduk DM, Loretto MH, editors. Gamma titanium aluminides. Warrendale, USA: TMS; 1999. p. 371.

[20] Bystrzanowski S. Creep behavior and microstructure stability of the Ti-46Al-9Nb sheet material. Aachen, Germany: Shaker Verlag; 2005.

[21] Yeoh LA, Liss KD, Bartels A, Chladil HF, Avdeev M, Clemens H, Gerling R, Buslaps T. Scripta Materialia 2007; 57: 1145.

[22] Bendersky LA, Boettinger WJ, Burton BP, Biancaniello FS, Shoemaker, CB. Acta Metall Mater 1990; 38: 931.

[23] Yu TH, Koo CH. Mater Sci Eng 1997; A239-240: 694.

[24] Stark A, Bartels A, Clemens H, Schimansky F-P. Adv Eng Mater 2008; 10: 929.

[25] Sikka SK, Vohra YK, Chidambaran R. Progress in Mater Sci 1982; 27: 245.

[26] Bartels A, Schillinger W. Intermetallics 2001; 9: 883.

[27] Mecking H. In: Wenk HR, editor. Preferred Orientation in Deformed Metals and Rocks: An Introduction to Modern Texture Analysis. Orlando: Academic Press; 1985.

[28] Los Alamos polycrystal plasticity Code, Los Alamos National Lab. LA-CC-88-6, Los Alamos, NM 87545, USA

[29] Mecking H, Hartig Ch, Kocks UF. Acta Mater 1996; 44: 1309.

[30] Bishop JFW, Hill R. Phil Mag 1951; 42: 1298.

**Figure and Table Captions**

Table 1:

Tensile test conditions and corresponding pole figures of the tested specimen.

Figure 1:

Representative microstructures which are developed in Ti-46Al-9Nb sheet material during tensile tests at different temperatures and at a constant strain rate of $1\times10^{-4}$ $s^{-1}$; (a, b) initial condition; (c, d) T = 750°C, $\varepsilon = 0.05$ (in (c) mechanical twins are marked by arrows); (e, f) T = 850°C, $\varepsilon = 0.46$ (note that in (f) some deformation-induced pores are present); (g, h) T = 1000°C, $\varepsilon = 0.65$. All pictures were taken from the uniformly deformed part of the specimens. LM (left) and SEM-BSE (right). Tensile direction is vertical.

Figure 2:

Microstructures in Ti-46Al-9Nb sheet material after tensile testing at 950°C applying two different strain rates. Both specimens were equally elongated to a plastic strain of ~0.47. Strain rate $1\times10^{-3}$ $s^{-1}$: (a) uniformly elongated gauge area; (c) necking-zone. Strain rate $1\times10^{-4}$ $s^{-1}$: (b) uniformly elongated gauge area, (d) necking-zone. Tensile direction is vertical.

Figure 3:

X-ray diffraction patterns (a) from an untested tensile specimen; (b) from the stressed part after tensile test at 750°C with a strain rate of $1\times10^{-5}$ $s^{-1}$ (shifted by 1° and 2000 counts) and (c) of the unstressed head of the sample (shifted by 2° and 4000 counts). The diffraction peaks of the initial material are assigned to the $\alpha_2$- and $\gamma$- phases. The presence of the ordered $\omega$-phase is indicated by the peaks $\omega/B8_2$-(110) at $2\Theta = 39.3°$ and $\omega/B8_2$-(102) at 39.7°.

Figure 4:

Conditions under which the ω/$B8_2$-phase could be identified in the gauge area of differently tested tensile specimens by means of X-ray diffraction. The time denotes the duration of the respective tensile test experiment, conducted at different strain rates, until failure.

Figure 5:

SEM images in BSE mode of the microstructure of a sample which has been tensile tested at 750°C and a strain rate of $1x10^{-5}$ $s^{-1}$. Top: unstressed head of the test specimen; bottom: stressed gauge area of the sample. The arrows in the bottom image indicate the ω/$B8_2$-phase particles.

Figure 6:

Texture development of γ-TiAl (space group: P4/mmm) after tensile deformation in Ti-46Al-9Nb sheet material with near gamma microstructure as function of temperature and strain rate (see also table 1). The prevailing texture is represented in form of inverse pole figures in tensile direction. A comprehensive description is given in the text. The previous RD of the starting sheet material is always parallel to the tensile direction of the experiments.

Figure 7:

Recalculated γ-001 and γ-111 pole figures of (a) the starting sheet material and (b,c) after tensile deformation at 750°C. TD = tensile direction of the experiments (it is parallel to the previous RD of the starting sheet material). Dashed lines show rotation symmetric positions around the TD.

Figure 8:

(a,b) Simulated orientation flow of γ-TiAl (space group: P4/mmm) during tensile deformation calculated with the LApp code using CRSS ratios of $\tau_o/\tau_s$ = 0.9 and $\tau_t/\tau_s$ = 0.4. Orientation flow map for (a) ε = 0.00 – 0.02 and (b) ε = 0.02 – 0.04, note also the flow towards <001> due to mechanical twinning (long arrows). (c) Experimental result. The tensile test parameters are given in the inset.

**Tables**

| Temperature [°C] | Strain rate [$s^{-1}$] | True fracture strain | Inverse pole figure in Fig. 6 |
|---|---|---|---|
| PA-Initial condition | | | a |
| 700 | $1 \cdot 10^{-5}$ | 0.07 | b |
| | $3 \cdot 10^{-6}$ | 0.12 | |
| | $1 \cdot 10^{-6}$ | 0.18 | c |
| 750 | $1 \cdot 10^{-4}$ | 0.05 | d |
| | $3 \cdot 10^{-5}$ | 0.15 | e |
| | $1 \cdot 10^{-5}$ | 0.42 | f |
| 800 | $1 \cdot 10^{-3}$ | 0.04 | |
| | $1 \cdot 10^{-4}$ | 0.42 | |
| | $3 \cdot 10^{-5}$ | 0.46 | |
| 850 | $1 \cdot 10^{-3}$ | 0.45 | g |
| | $3 \cdot 10^{-4}$ | 0.55 | h |
| | $1 \cdot 10^{-4}$ | 0.46 | i |
| 900 | $1 \cdot 10^{-3}$ | 0.49 | j |
| | $3 \cdot 10^{-4}$ | 0.47 | k |
| | $1 \cdot 10^{-4}$ | 0.51 | l |
| 950 | $1 \cdot 10^{-3}$ | 0.47 | m |
| | $3 \cdot 10^{-4}$ | 0.52 | n |
| | $1 \cdot 10^{-4}$ | 0.48 | o |
| 1000 | $1 \cdot 10^{-3}$ | 0.63 | p |
| | $3 \cdot 10^{-4}$ | 0.45 | q |
| | $1 \cdot 10^{-4}$ | 0.65 | r |

Table 1

**Figures**

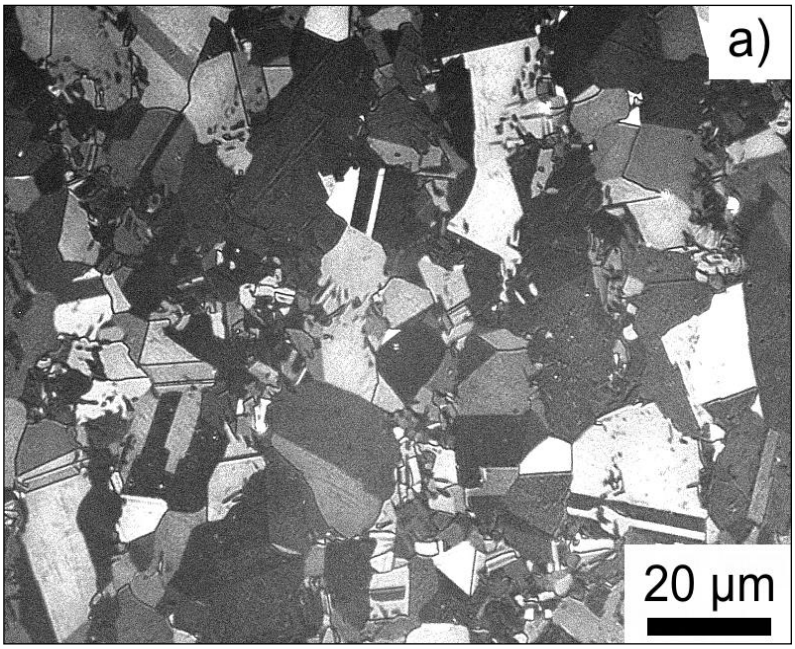


Figure 1a

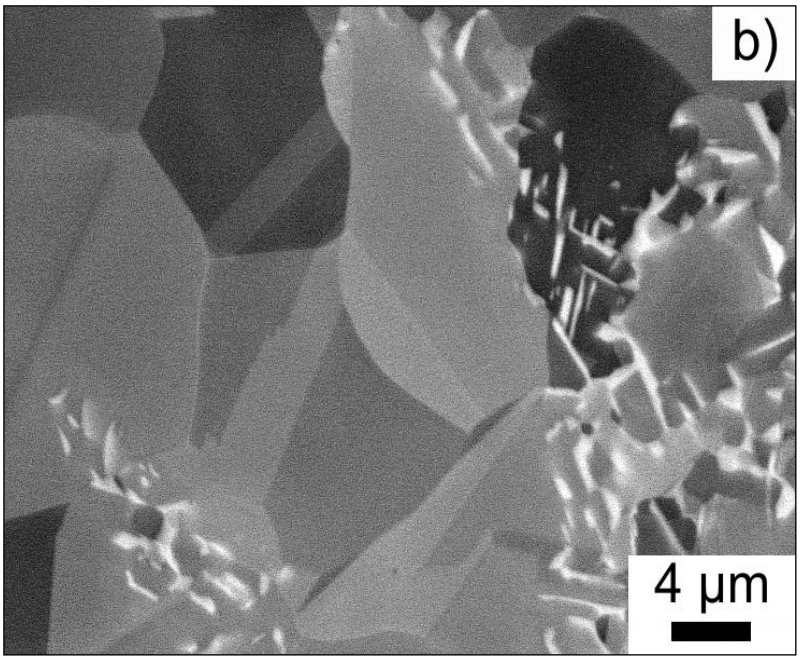

Figure 1b

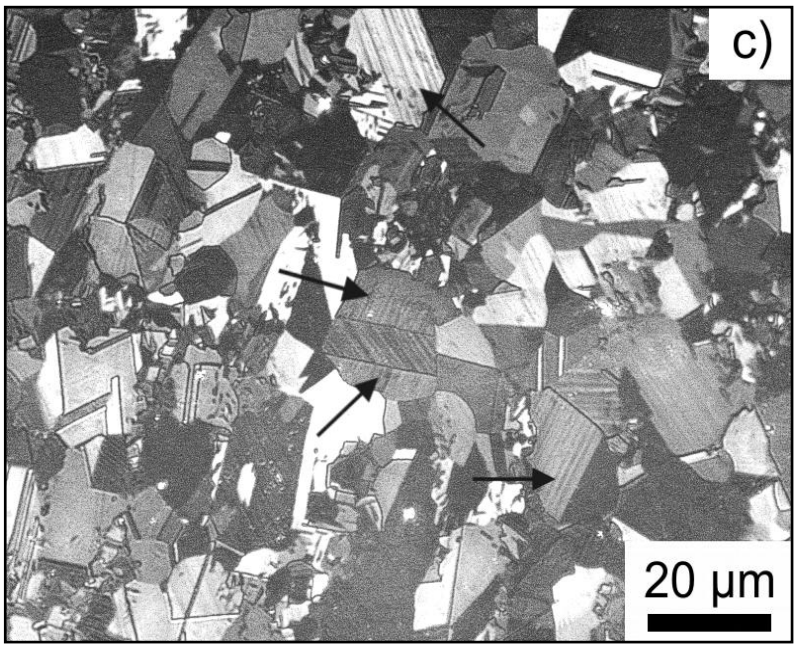


Figure 1c

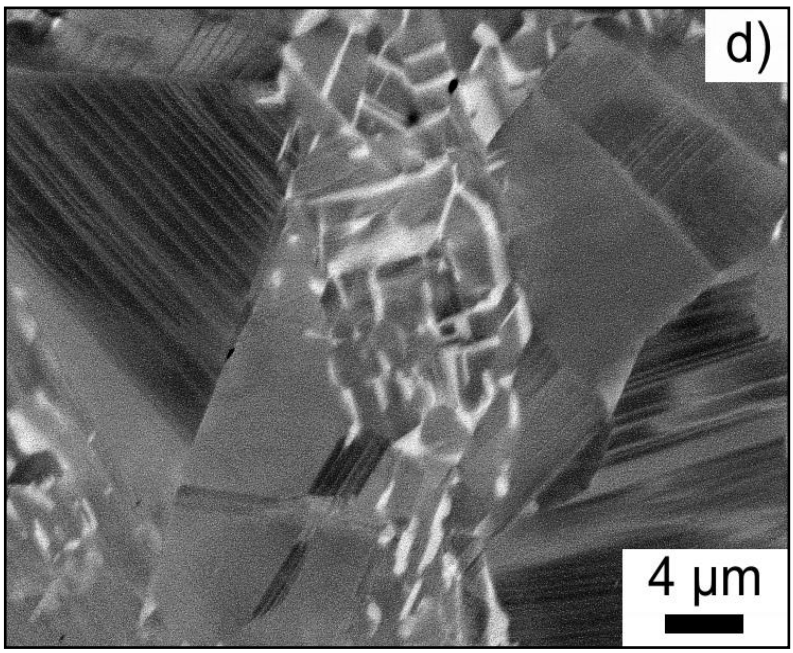


Figure 1d

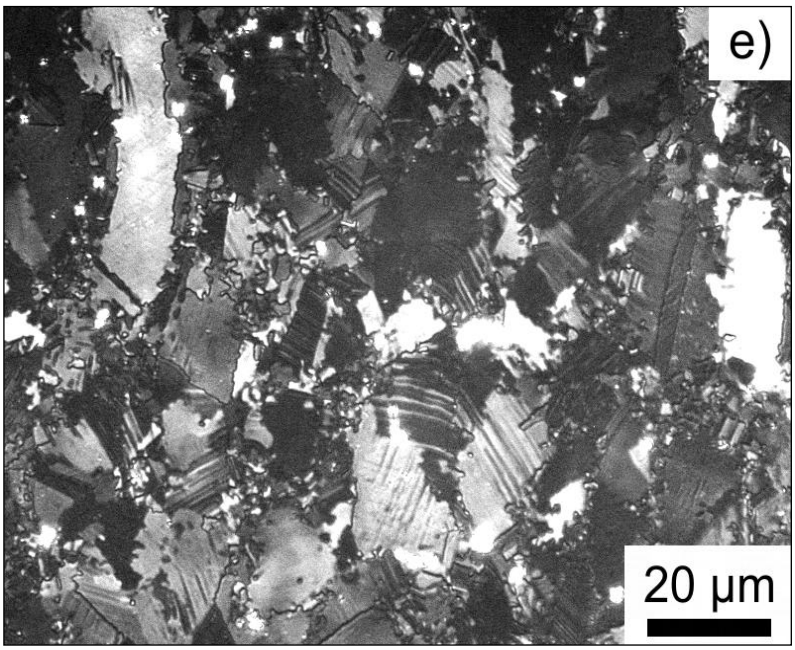


Figure 1e

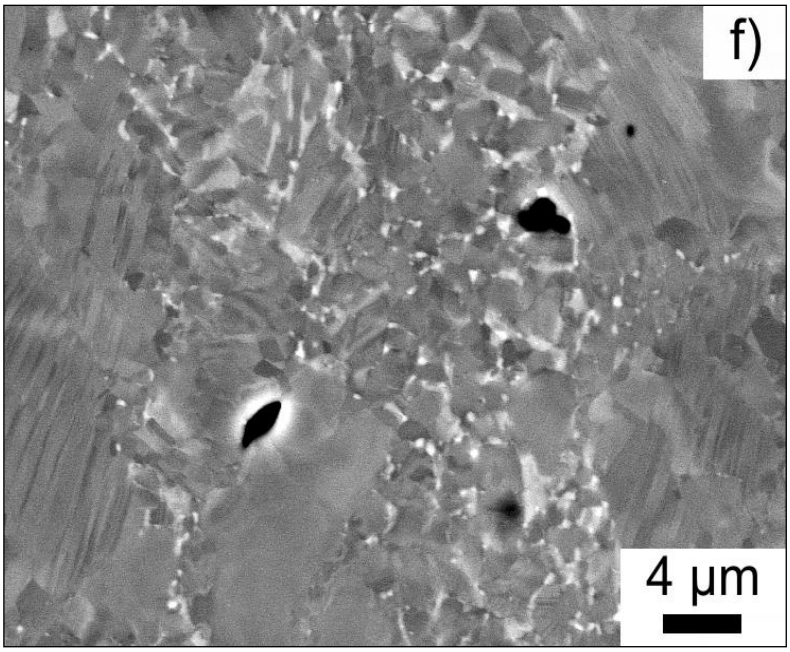


Figure 1f

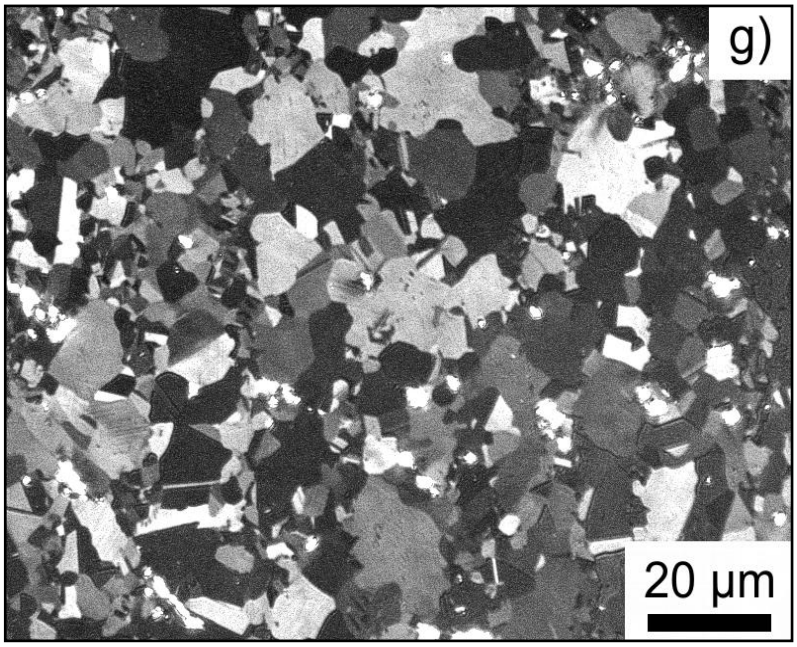


Figure 1g

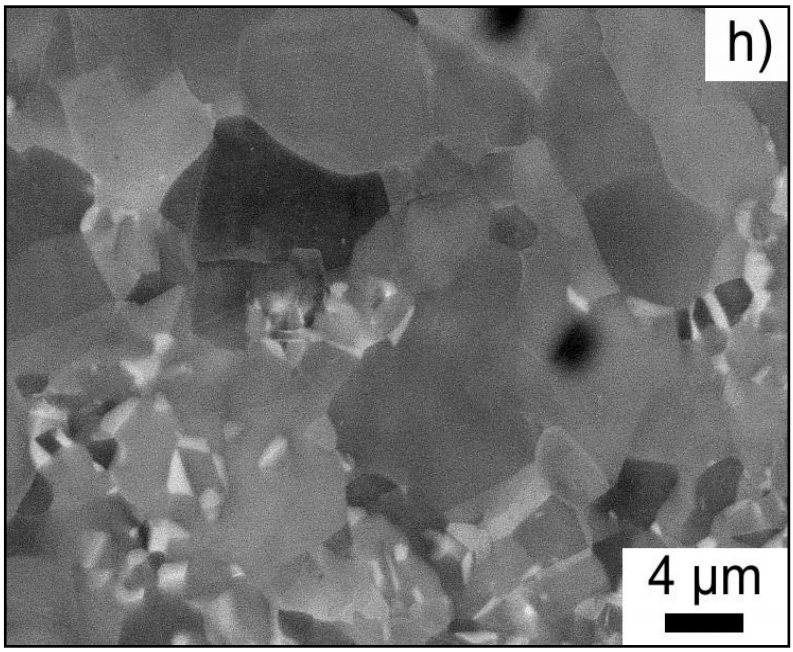


Figure 1h

Layout sketch of figure 1:

Please arrange the figures of figure 1 according to the following rough layout:

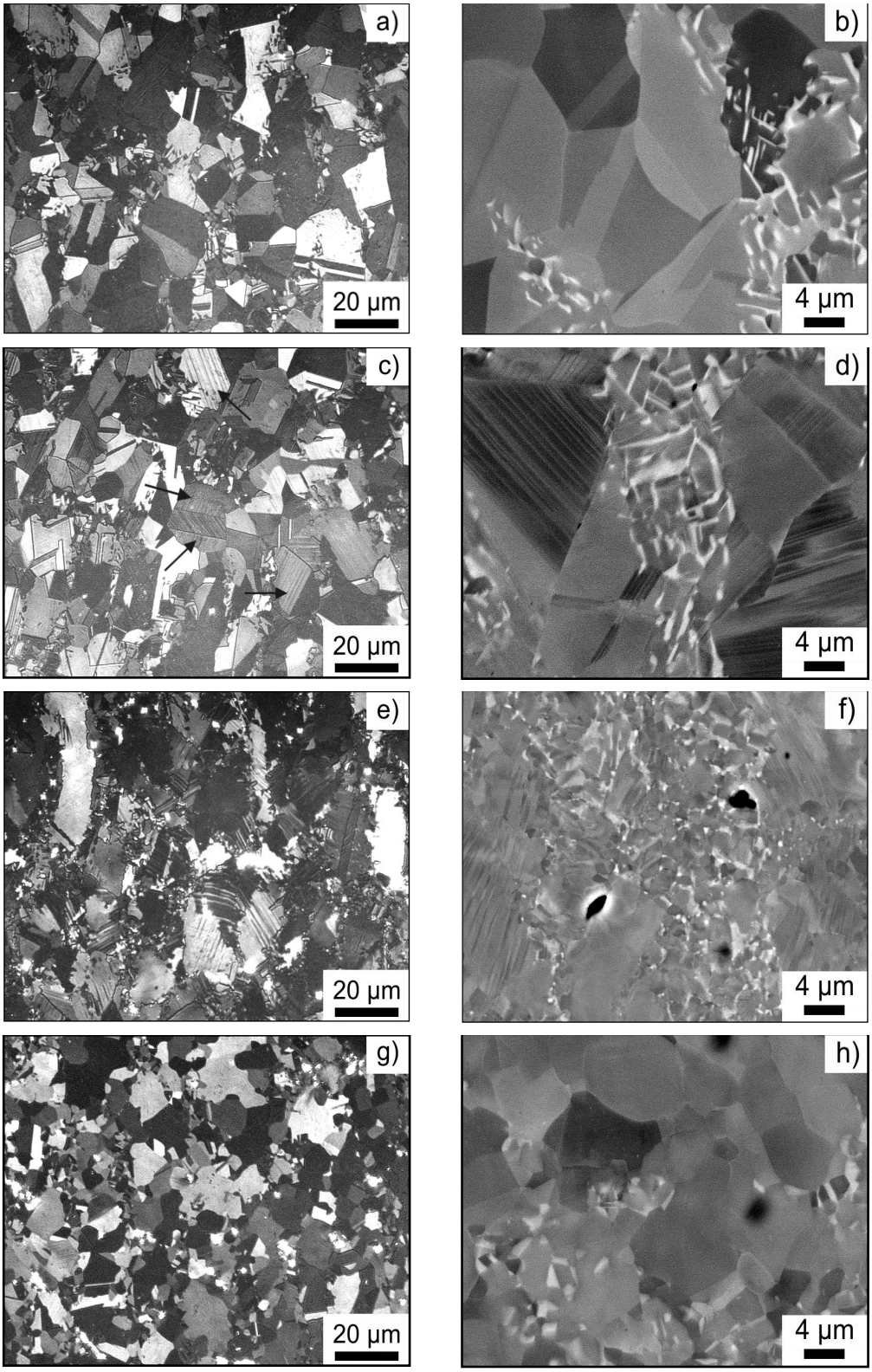

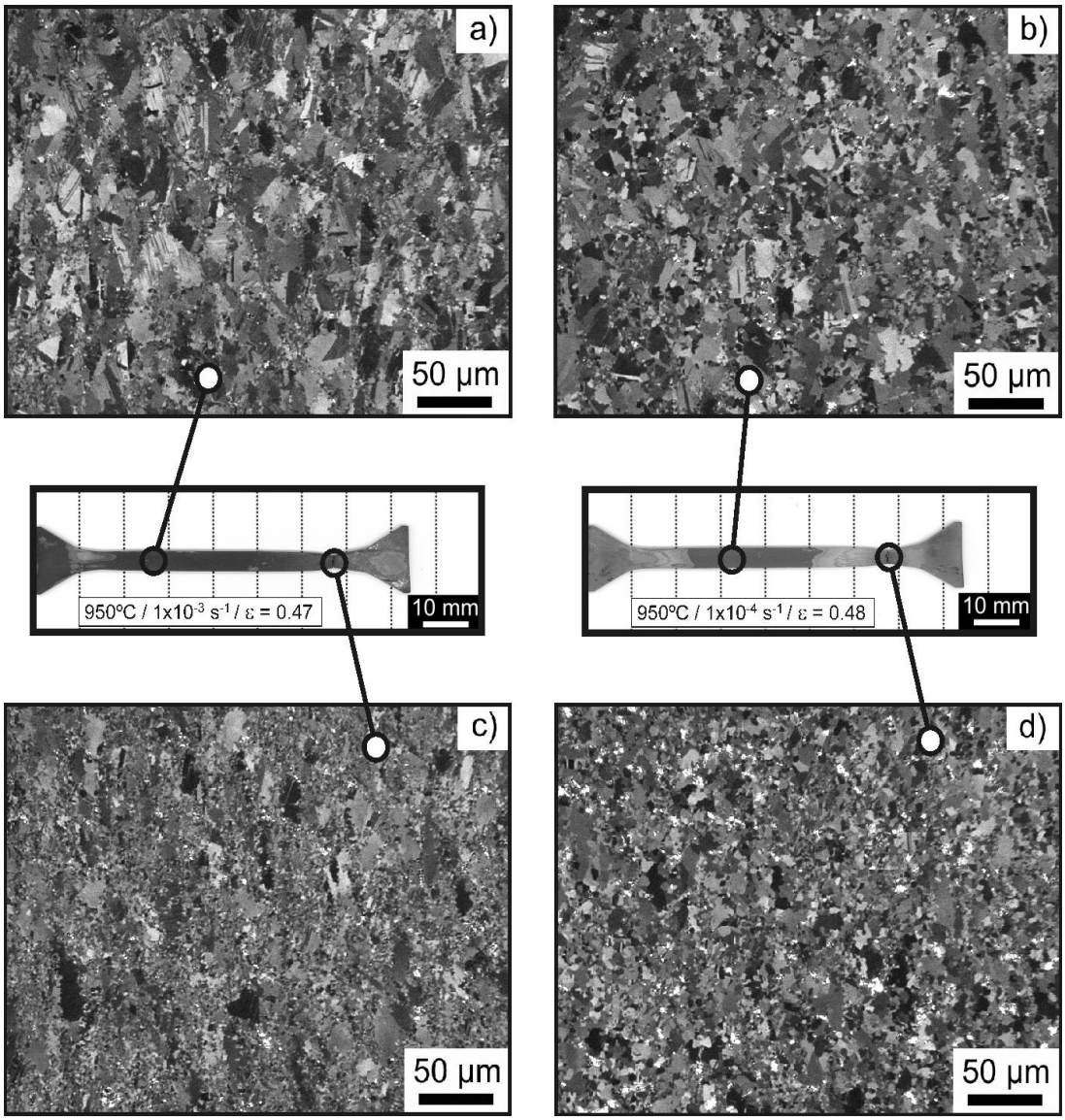
a)
50 µm
b)
50 µm
950°C / 1x10-3 s-1 / ε = 0.47
10 mm
950°C / 1x10-4 s-1 / ε = 0.48
10 mm
c)
50 µm
d)
50 µm

Figure 2

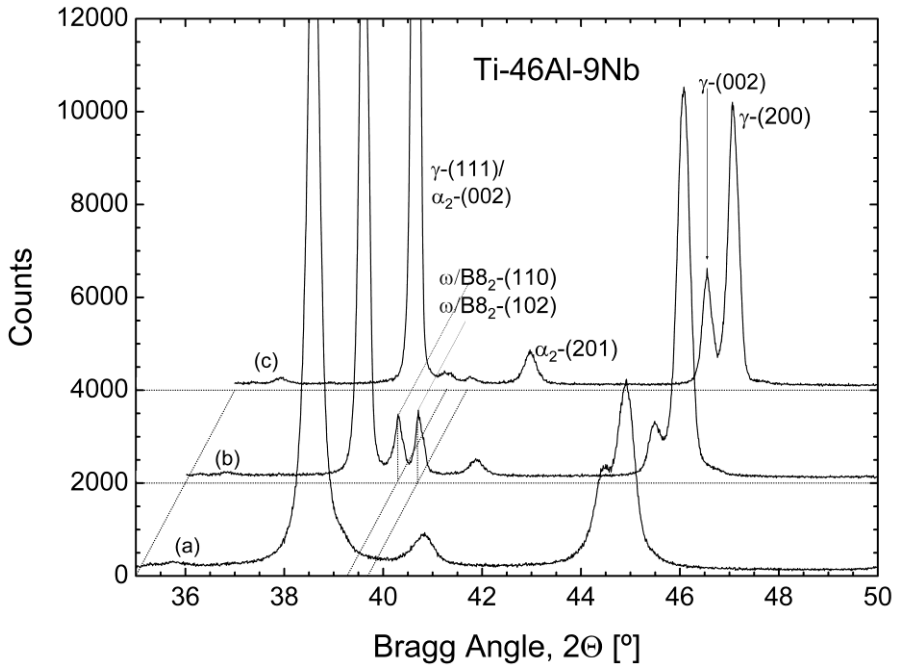
Ti-46Al-9Nb
γ-(002)
γ-(200)
γ-(111)/
α2-(002)
ω/B82-(110)
ω/B82-(102)
α2-(201)
(c)
(b)
(a)
Counts
Bragg Angle, 2Θ [º]
0
2000
4000
6000
8000
10000
12000
36
38
40
42
44
46
48
50

Figure 3

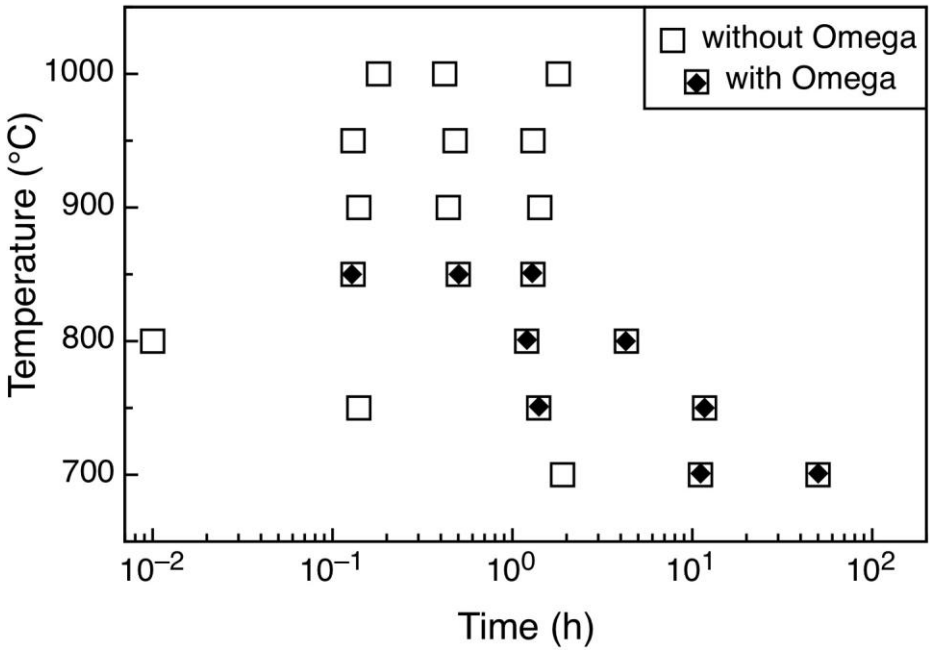
without Omega
with Omega
1000
900
800
700
Temperature (°C)
$10^{-2}$
$10^{-1}$
$10^{0}$
$10^{1}$
$10^{2}$
Time (h)

Figure 4

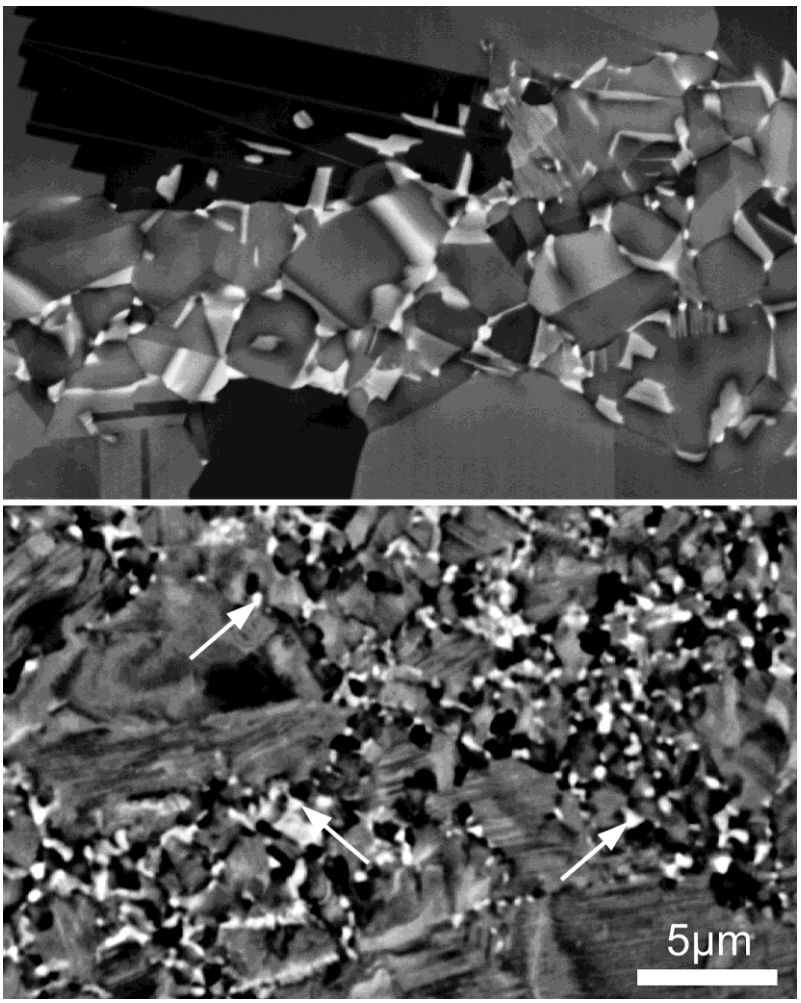


Figure 5

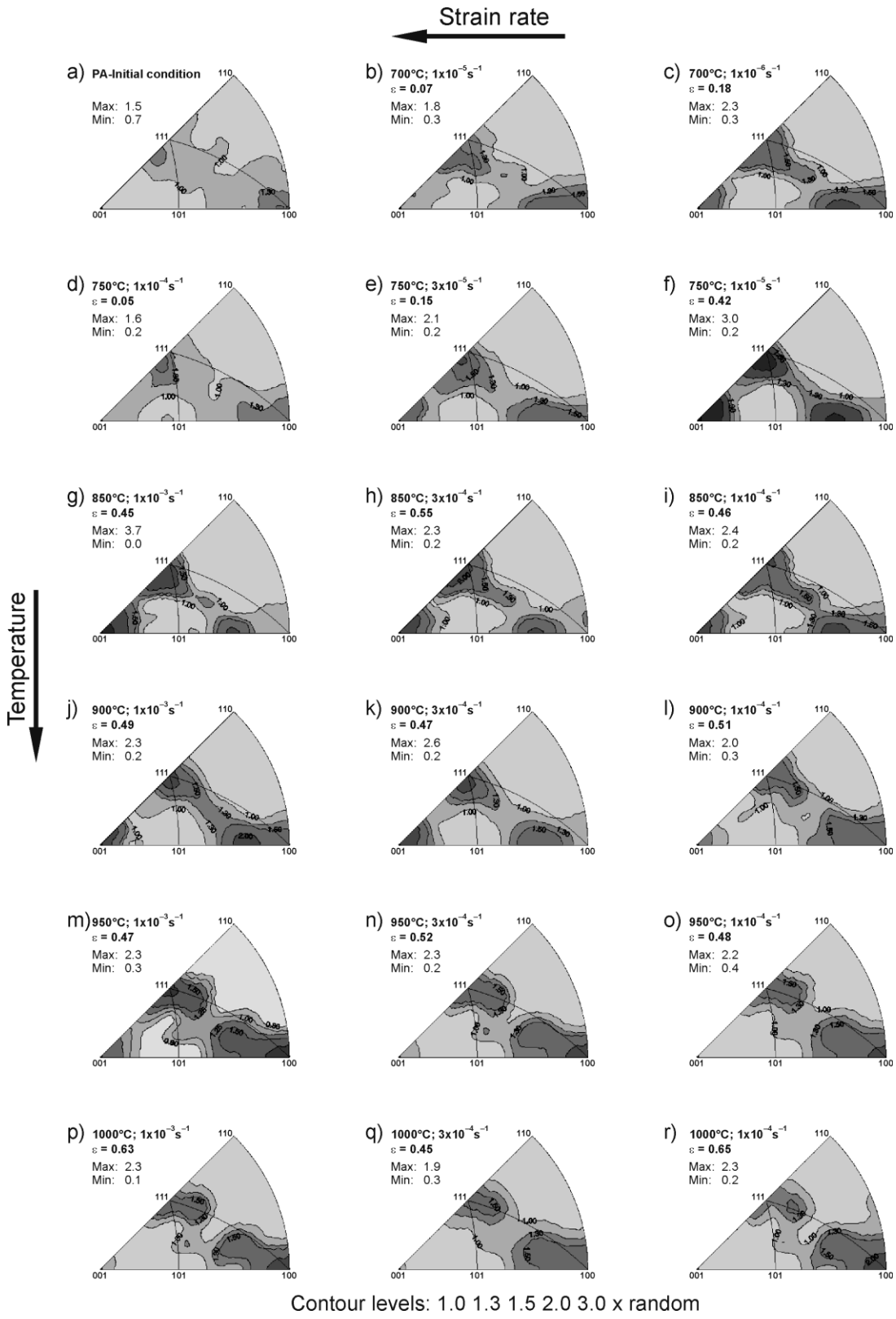
Strain rate
Temperature
a) PA-Initial condition
Max: 1.5
Min: 0.7
b) 700°C; 1x10⁻⁵s⁻¹
ε = 0.07
Max: 1.8
Min: 0.3
c) 700°C; 1x10⁻⁶s⁻¹
ε = 0.18
Max: 2.3
Min: 0.3
d) 750°C; 1x10⁻⁴s⁻¹
ε = 0.05
Max: 1.6
Min: 0.2
e) 750°C; 3x10⁻⁵s⁻¹
ε = 0.15
Max: 2.1
Min: 0.2
f) 750°C; 1x10⁻⁵s⁻¹
ε = 0.42
Max: 3.0
Min: 0.2
g) 850°C; 1x10⁻³s⁻¹
ε = 0.45
Max: 3.7
Min: 0.0
h) 850°C; 3x10⁻⁴s⁻¹
ε = 0.55
Max: 2.3
Min: 0.2
i) 850°C; 1x10⁻⁴s⁻¹
ε = 0.46
Max: 2.4
Min: 0.2
j) 900°C; 1x10⁻³s⁻¹
ε = 0.49
Max: 2.3
Min: 0.2
k) 900°C; 3x10⁻⁴s⁻¹
ε = 0.47
Max: 2.6
Min: 0.2
l) 900°C; 1x10⁻⁴s⁻¹
ε = 0.51
Max: 2.0
Min: 0.3
m) 950°C; 1x10⁻³s⁻¹
ε = 0.47
Max: 2.3
Min: 0.3
n) 950°C; 3x10⁻⁴s⁻¹
ε = 0.52
Max: 2.3
Min: 0.2
o) 950°C; 1x10⁻⁴s⁻¹
ε = 0.48
Max: 2.2
Min: 0.4
p) 1000°C; 1x10⁻³s⁻¹
ε = 0.63
Max: 2.3
Min: 0.1
q) 1000°C; 3x10⁻⁴s⁻¹
ε = 0.45
Max: 1.9
Min: 0.3
r) 1000°C; 1x10⁻⁴s⁻¹
ε = 0.65
Max: 2.3
Min: 0.2
110
111
001
101
100
Contour levels: 1.0 1.3 1.5 2.0 3.0 x random

Figure 6

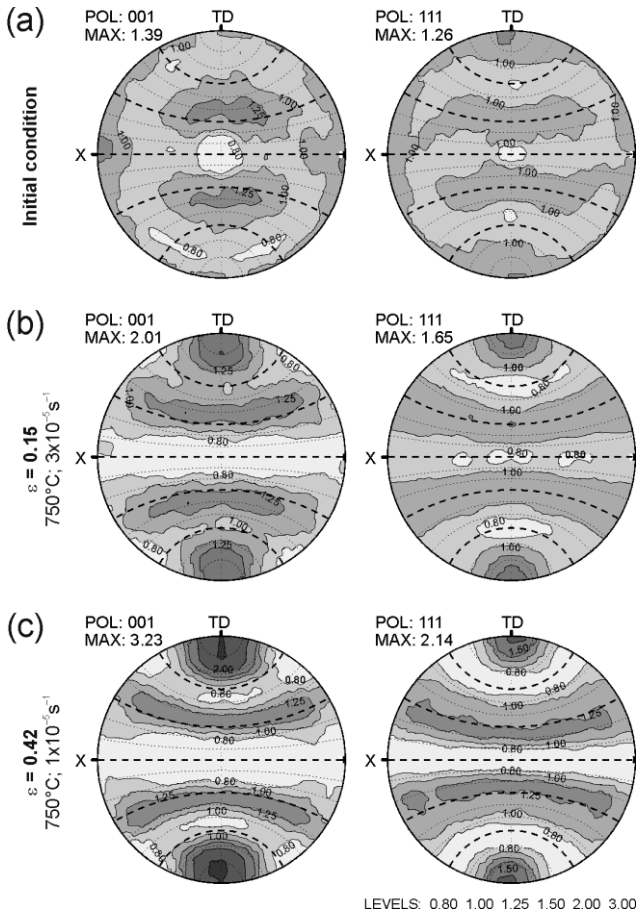
(a)
POL: 001
MAX: 1.39
TD
POL: 111
MAX: 1.26
TD
Initial condition
X
X
(b)
POL: 001
MAX: 2.01
TD
POL: 111
MAX: 1.65
TD
ε = 0.15
750°C; 3x10⁻⁵ s⁻¹
X
X
(c)
POL: 001
MAX: 3.23
TD
POL: 111
MAX: 2.14
TD
ε = 0.42
750°C; 1x10⁻⁵ s⁻¹
X
X
LEVELS: 0.80 1.00 1.25 1.50 2.00 3.00

Figure 7

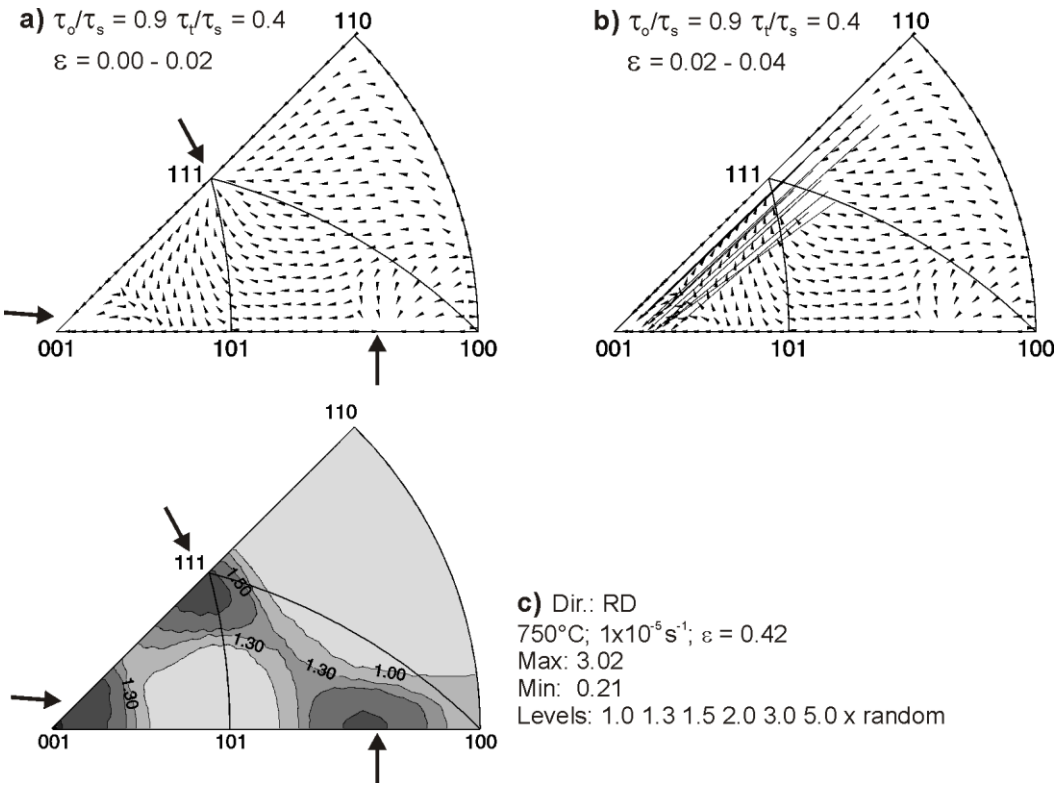
a) $\tau_o/\tau_s$ = 0.9 $\tau_t/\tau_s$ = 0.4
ε = 0.00 - 0.02
110
111
001
101
100
b) $\tau_o/\tau_s$ = 0.9 $\tau_t/\tau_s$ = 0.4
ε = 0.02 - 0.04
110
111
001
101
100
110
111
1.60
1.30
1.30
1.00
1.30
001
101
100
c) Dir.: RD
750°C; 1x10$^{-5}$s$^{-1}$; ε = 0.42
Max: 3.02
Min: 0.21
Levels: 1.0 1.3 1.5 2.0 3.0 5.0 x random

Figure 8